Data Repository 2009150: Cowgill et al., Altyn Tagh Slip Rate

Methods & sample characteristics:

We used a Leica TCR407power total station linked to an iPAQ computer running Microsurvey FieldGenius software to survey the site, including both breaklines along the edges of the main topographic features and topographic control points within the areas bounded by the breaklines. Following the survey, we excavated 1-2 m deep pits and collected radiocarbon samples that we stored in airtight containers until the end of fieldwork. We dug a total of 13 pits, 8 of which yielded a total of 35 dateable samples. On the T4 surface, 3 pits south of the fault yielded 22 dateable samples and 2 pits north of the fault were barren. On the T3 surface we dug 6 pits (3 upstream, 3 downstream) in loess deposits at the base of the T4/T3 riser and found 6 dateable samples. Two pits on T2 yielded 7 dateable samples. We excavated the pits at the riser bases on T3 and T2 (i.e., in the distal portions of the apron of loess and colluvium) to both ensure that our hand-dug and unsupported pits would expose the buried terrace tread and minimize the risk of either confusing colluvial layers with the underlying terrace or sampling organic material recycled from the overlying terrace. We did not analyze a suite of samples collected from T4 for exposure-age dating due to extensive loess cover. Before leaving the site, Cowgill mapped the area on ~1:5,000-scale stereo prints made from 7 micron scans of Corona images with ~1.8m ground resolution.

Samples collected for ^{14}C analysis were primarily woody plant fragments but also included charcoal and dung. The absence of animal burrows on the modern surface and the presence of undisrupted fine layering within the loess deposits both at the riser bases and on the terraces attest to minimal disturbance of the loess after burial of the organic material. Most samples were under 1 cm in diameter and very friable. The dung was identified based on elliptical shapes and powdery/fibrous texture. The woody fragments had shapes and textures similar to dead branches on modern plants in the area. These plants typically form the tops of 5-10 cm tall loess mounds, with dead branches commonly buried in the apron of sediment surrounding the plant. Thus, the plants appear to trap loess, with dead branches becoming buried as the plant grows up through the accreting sediment. This depositional model explains why the bulk of the sampled material was woody plant fragments. We conducted mechanical and chemical pretreatment of the samples at UC Davis following procedures described by Olsson (1986). At the W.M. Keck Carbon Cycle Accelerator Mass Spectrometry Laboratory (KCCAMS) at UC Irvine, we combusted the samples, extracted CO_2 gas, graphitized the samples, and packed targets prior to analysis. We processed samples of radiocarbon-dead wood and FIRI D and FIRI H standards with the unknowns.

Supplementary field observations:

Yuemake is located west of the left-stepping Akato Tagh restraining bend (Fig. DR1), the bedrock and neotectonic geology of which are described by Cowgill et al., (2004b) and Cowgill et al, (2004a), respectively. To the east of Yuemake channel, the ATF defines the northern margin of a bedrock range, and to the west it cuts a flight of alluvial terraces before crossing a fault-parallel ridge (Figs. DR2 and DR3). Holocene surface rupture of the ATF has been documented along this reach (Ge et al., 1992) and to both the west (Muretta et al., 2007) and east (Washburn et al., 2003; Washburn et al., 2001). Evidence at the site includes internally drained depressions along the fault, an uphill-facing fault scarp on T4, and channels on the east bank that are beheaded and/or left-deflected where they cross the fault (Fig. DR3A).

The fluvial terraces and their intervening risers are well-defined on the west bank, with the T4/T3 riser and flanking T4 and T3 terraces present both north and south of the fault (Figs. 2

and DR2-DR3). The T4/T3 riser crest is ~6 and ~14 m above the T3 surface and active channel, respectively. North of the fault, the riser is straight in plan view to within a few meters of the fault (Fig. DR3). To the south it terminates ~15 m from the fault, with the northernmost ~10 m section of the riser trending more westerly than sections farther south (Fig. DR3). This riser is truncated to the north by a north-facing scarp along the ATF. This scarp is both hummocky and cut by a tectonic furrow, indicating it as a minor slump formed by collapse of the free face of the T4 terrace into the modern drainage along the fault scarp (Figs. DR3 and DR4A).

The main riser faces are asymmetric in profile view, with steeper slopes at the crest than the base (Fig. DR4B). Conglomerates exposed at the riser crests are buried by laminated sand and loess at the base. Excavations at the bases of the T4/T3 and T3/T2 risers indicate that these fine-grained deposits extend 1-1.5 m below the modern surface and depositionally overly the flat-lying, cobbled surfaces of the T3 and T2 terraces. We interpret the fine-grained deposits to primarily reflect in situ accumulation of loess in the lee of the riser with minor reworking of material from the loess cap on the overlying terrace tread. Because these units depositionally overly both the face of the terrace riser and the lower terrace tread, they post-date fluvial abandonment of the riser. Therefore, radiocarbon samples within these deposits provide a minimum bound on the riser age.

With the exception of the active channel (T0 and T0'), all terrace surfaces are blanketed by deposits of loess and fine sand up to 2 m thick (Fig. DR4). Cutbank exposures south of the fault indicate T3 is a strath terrace, with up to ~1 m of stratified conglomerate and pebbly sands unconformably overlying fractured schist (Fig. DR4C). Bedrock is also exposed within the active drainage (T0-T0'), ~200 m south of the fault. However, it is unclear if other terraces in the area are straths.

The T4 and T3 terrace surfaces on the west bank of the Yuemake channel and north of the fault are bowed vertically upwards by several meters within ~100 m of the fault, with higher terraces most strongly arched. Two types of discontinuous, ~1 m high secondary scarps are spatially associated with the crests of the main T4/T3 and T3/(T2-T1) risers. The first are fluvial risers that only occur north of the fault. The second lie above the main riser crest in areas where the treads are overlain by post-abandonment loess deposits and are defined by slope breaks in the loess. At least three older/higher terraces (T5-T7) are also present at Yuemake (Fig. DR3A). Although Cowgill et al., (2004a) mapped a secondary fault along these northwest-facing scarps based on analysis of Corona imagery, our more recent field observations indicate that these scarps are simply older fluvial terrace risers.

Additional discussion of Holocene displacement:

We used the T4/T3 riser crest to determine displacement because the midpoint was obscured by loess (e.g., Fig. DR4B). When projecting the riser (Figs. 2 and DR3B) we ignored the curved riser segment that is ~10 m long at the north end of the southern riser, which we attribute to local drainage deflection prior to T3 abandonment. Inclusion of this segment would lower the total offset and thus reduce the slip rate. More northerly trending riser projections leading to larger total offset and thus faster rates are not supported by the survey data and site geomorphology (Fig. DR3c). Such projections do not follow the riser crest or any other topographic feature within the riser. In addition, they do not mimic the margins of the modern flood plain (e.g., T0/T1 riser) in terms of the amplitude and wavelength of riser sinuosity or overall riser trend direction. The projections we show span the range of riser trends seen along T3/T4 north of the fault and along other risers at the site. Thus, restoration of fault slip returns the projected riser to a geometry that match patterns seen elsewhere at the site, both along other portions of the T3/T4 riser and along other risers.

The total slip of 54±5 m recorded by the T4/T3 riser is broadly similar to a less-precise offset determination derived from reconstructing the T4 terrace surface. Because this surface slopes oblique to the fault trace, sinistral displacement along the fault has juxtaposed higher elevations on the T4 terrace to the north against lower elevations to the south, producing the uphill-facing fault scarp and systematic left steps in the topographic contours where they cross the fault trace (Figs. 2 and DR3B). These steps can be used to estimate total slip since T4 abandonment. Specifically, ~64 m of pure left slip restores the jog in the 950 m contour line However, this total slip measurement is less accurate than that based on the riser because it presumes that separation of the T4 topographic surface was only due to strike-slip displacement and does not account for changes in T4 elevation due to erosion, loess accumulation, or deformation.

Details regarding ^{14}C results:

Table DR1 reports results of 40 radiocarbon analyses, including 35 unknowns and 5 replicates to check reproducibility. The 35 unknowns comprise 28 from the T3 and T4 terraces to bracket the T4/T3 riser age and 7 from T2, to test for stratigraphic order. Results are plotted in Figures 2 and DR5. Analyses are standard accelerator mass spectrometer (AMS) measurements made at KCCAMS. Radiocarbon concentrations are given as fractions of the Modern standard, $D^{14}C$, and conventional radiocarbon age, following conventions of Stuiver and Polach (1977). All results have been corrected for isotopic fractionation according to the conventions of Stuiver and Polach (1977), with $\delta^{13}C$ values measured on prepared graphite using the accelerator mass spectrometer. These can differ from $\delta^{13}C$ of the original material, if fractionation occurred during sample graphitization or AMS measurement, and are not shown.

We calibrated calendar dates using OxCal v.4.0.1 (Bronk Ramsey, 1995, 2001) and the IntCal04 (Reimer et al., 2004) atmospheric calibration curve. Age ranges are reported at 2σ and are plotted on the age-depth plots (Figs. 2 and DR5) as bars spanning the total 2σ range of the probability density function for the calibrated age. Because the thickness of the post-abandonment loess varies between excavations, we normalized sample depths by the total thickness of loess in each pit. This approach assumes that loess thickness variations stem from spatial variations in accumulation rate, and that deposition at each pit was either uniform over time, or that temporal variations affected all pits uniformly. The samples generally plot in correct stratigraphic order, supporting this assumption.

Details of Slip Rate Calculations:

Numerous studies have discussed methods for combining age and offset measurements from displaced fluvial risers to determine slip rates (Cowgill, 2007; England and Molnar, 2005; Harkins and Kirby, 2008; Mériaux et al., 2004; Mériaux et al., 2005; Van der Woerd et al., 1998; Van der Woerd et al., 2002; Zhang et al., 2007). We used the most conservative approach by accounting for the full range of possible riser ages (Cowgill, 2007). In particular, we use the abandonment ages of both the lower (T3) and upper (T4) terraces to bracket the age of riser formation and thus place maximum and minimum bounds on the slip rate, respectively. We calculated uncertainties on these bounding rates by propagating the uncertainties in the displacement and terrace abandonment ages as the square-root of the sum of the squares, normalizing each uncertainty by the mean value. The upper bound on the rate is a true maximum because we have bracketed the T3 abandonment age. The true minimum rate could be lower than 9.4±0.9 mm/yr if abandonment of T4 and formation of the T4/T3 riser significantly predated the oldest ^{14}C samples contained within the T4 loess cap.

Table DR1: Results of Radiocarbon Analyses

UCI AMS #	Depth (cm)	Fractional Depth[◊]	Sample Name[‡]	Stratigraphic context	Material	Fraction Modern	±	$D^{14}C$	±	^{14}C age (years BP)	±	Calibrated Age Range[§] (calBP)
26476	37	0.25	05S1T2NA-C05	in loess cap	wood	0.7803	0.0013	-219.7	1.3	1990	15	1990 to 1895
26477	46	0.32	05S1T2NA-C03a[†]	in loess cap	wood	0.7716	0.0014	-228.4	1.4	2085	15	2115 to 1999
26478	"	"	05S1T2NA-C03b[†]	in loess cap	wood	0.7738	0.0012	-226.2	1.2	2060	15	2111 to 1952
26479	75	0.51	05S1T2NA-C04	in loess cap	modern root?	0.7966	0.0013	-203.4	1.3	1825	15	1817 to 1717
20514	156	1.07	05S1T2NA-C02[†]	in terrace	wood	0.7337	0.0012	-266.3	1.2	2490	15	2714 to 2488
26480	"	"	05S1T2NA-C02[†]	"	"	0.7323	0.0011	-267.7	1.1	2500	15	2717 to 2493
26481	162	1.11	05S1T2NA-C01	in terrace	wood	0.7489	0.0012	-251.1	1.2	2325	15	2354 to 2334
26482	26	0.19	05S1T2NB-C02	in loess cap	wood	0.7912	0.0012	-208.8	1.2	1880	15	1877 to 1739
26483	47	0.34	05S1T2NB-C01	in loess cap	wood	0.7651	0.0016	-234.9	1.6	2150	20	2301 to 2060
20513	95.8	0.87	05S1T3NA-C01	in loess cap	wood	0.6387	0.0026	-361.3	2.6	3600	35	4065 to 3830
26452	121	1.03	05S1T3SA-C04	in terrace	wood	0.6373	0.0024	-362.7	2.4	3620	30	4068 to 3842
26453	123	1.05	05S1T3SA-C01	in terrace	wood	0.6323	0.0014	-367.7	1.4	3685	20	4089 to 3931
26454	129	1.10	05S1T3SA-C03	in terrace	wood	0.6019	0.0021	-398.1	2.1	4080	30	4806 to 4444
26455	43	0.46	05S1T3SB-C01	in loess cap	wood	0.6953	0.0020	-304.7	2.0	2920	25	3200 to 2969
26456	69	0.74	05S1T3SB-C03	in loess cap	wood	0.6642	0.0023	-335.8	2.3	3285	30	3585 to 3443
26484	70	0.79	05S1T4SA-C02	in loess cap	charcoal	0.5728	0.0011	-427.2	1.1	4475	20	5284 to 4980
26485	75	0.84	05S1T4SA-C01	in loess cap	charcoal	0.5699	0.0010	-430.1	1.0	4515	15	5299 to 5053
20511	75	0.84	05S1T4SA-C05[†]	in loess cap	charcoal	0.5732	0.0013	-426.8	1.3	4470	20	5282 to 4978
26486	"	"	05S1T4SA-C05[†]	"	"	0.5724	0.0010	-427.6	1.0	4480	15	5284 to 5041
20510	75	0.84	05S1T4SA-C06[†]	in loess cap	charcoal	0.5722	0.0009	-427.8	0.9	4485	15	5284 to 5044
26487	"	"	05S1T4SA-C06[†]	"	"	0.5720	0.0010	-428.0	1.0	4490	15	5286 to 5046
26488	77	0.87	05S1T4SA-C03	in loess cap	charcoal	0.5698	0.0011	-430.2	1.1	4520	20	5303 to 5053
26489	78	0.88	05S1T4SA-C04	in loess cap	charcoal	0.5710	0.0010	-429.0	1.0	4500	15	5288 to 5050
26436	44	0.33	05S1T4SB-C06	in loess cap	wood	0.8306	0.0014	-169.4	1.4	1490	15	1406 to 1340
26437	68	0.51	05S1T4SB-C05	in loess cap	wood	0.6660	0.0012	-334.0	1.2	3265	15	3557 to 3447
20512	75.5	0.57	05S1T4SB-C04[†]	in loess cap	wood	0.6293	0.0020	-370.7	2.0	3720	30	4151 to 3980
26438	"	"	05S1T4SB-C04[†]	"	"	0.6258	0.0021	-374.2	2.1	3765	30	4236 to 3998

26439	78	0.59	05S1T4SB-C03	in loess cap	dung	0.6178	0.0012	-382.2	1.2	3870	20	4412 to 4236
26440	80	0.60	05S1T4SB-C02	in loess cap	dung	0.5989	0.0011	-401.1	1.1	4120	20	4812 to 4530
26441	106	0.80	05S1T4SB-C01	in loess cap	dung	0.5357	0.0015	-464.3	1.5	5015	25	5889 to 5658
26442	21	0.22	05S1T4SC-C10	in loess cap	wood	0.8599	0.0014	-140.1	1.4	1215	15	1225 to 1068
26443	38	0.40	05S1T4SC-C11i	in loess cap	modern root?	1.0643	0.0017	64.3	1.7	-495	15	failed
26444	38	0.40	05S1T4SC-C11ii	in loess cap	wood	0.7614	0.0048	-238.6	4.8	2190	60	2340 to 2042
26445	41	0.43	05S1T4SC-C09i	in loess cap	modern root?	0.9194	0.0041	-80.6	4.1	675	40	685 to 556
26446	51	0.53	05S1T4SC-C08	in loess cap	wood?	0.6060	0.0012	-394.0	1.2	4025	20	4529 to 4424
26447	59	0.61	05S1T4SC-C06	in loess cap	wood?	0.6280	0.0090	-372.0	9.0	3740	120	4432 to 3730
26448	69	0.72	05S1T4SC-C05	in loess cap	wood	0.5770	0.0030	-423.0	3.0	4415	45	5278 to 4863
26449	74	0.77	05S1T4SC-C04	in loess cap	wood	0.5324	0.0029	-467.6	2.9	5065	45	5915 to 5665
26450	78	0.81	05S1T4SC-C03	in loess cap	wood	0.5342	0.0080	-465.8	8.0	5040	130	6177 to 5484
26451	81	0.84	05S1T4SC-C02	in loess cap	wood	0.6227	0.0030	-377.3	3.0	3805	40	4406 to 4084

Analyses are standard accelerator mass spectrometer (AMS) measurements from the UCI Keck Carbon Isotope Facility. Radiocarbon concentrations are given as fractions of the Modern standard, D14C, and conventional radiocarbon age, following the conventions of Stuiver and Polach (Radiocarbon, v. 19, p.355, 1977). Size-dependent sample preparation backgrounds have been subtracted based on measurements of ^{14}C-free wood. All results have been corrected for isotopic fractionation according to the conventions of Stuiver and Polach (1977), with δ13C values measured on prepared graphite using the accelerator mass spectrometer. These can differ from δ13C of the original material, if fractionation occurred during sample graphitization or the AMS measurement, and are not shown.

◊Fractional depths were calculated by dividing the sample depth by the total depth to the tread top (depths measured below present surface).

‡Key to sample name: year (2005), site (site #1), terrace number (T2, T3, or T4), position relative to fault trace (N = north, S = south), pit (A, B, or C), sample index. See maps in Figure DR3 for sample pit locations.

†Sample with replicate analyses.

§Calendar dates were calibrated using OxCal v4.0.1 (Bronk Ramsey, 2006) r:5 and the IntCal04 (Reimer et al. 2004) atmospheric curve. Age range is reported at 2σ

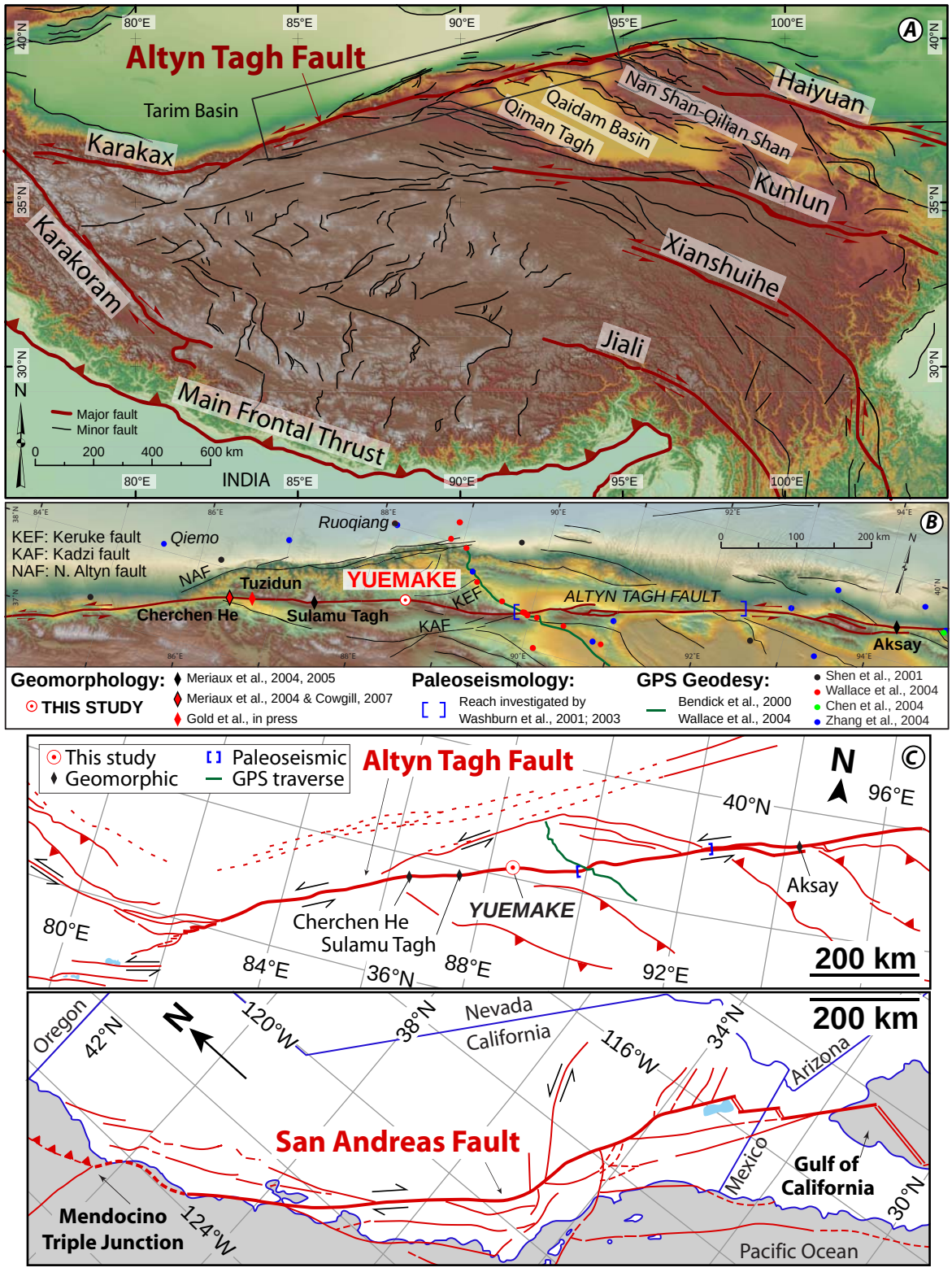

Figure DR1. (a) Map of the Indo-Asian collision showing major and minor faults based on compilation of Taylor et al. (2003) with additions from previous work (Cowgill et al., 2004b; Lacassin et al., 2004; Mériaux et al., 2004; Mériaux et al., 2005; Murphy and Burgess, 2006; Peltzer et al., 1989; Tapponnier et al., 2001; Thatcher, 2007; Yin et al., 2007). (b) Location along the central ATF of the Yuemake site, previous slip-rate studies (Bendick et al., 2000; Cowgill, 2007; Gold et al., in press; Mériaux et al., 2004; Mériaux et al., 2005; Wallace et al., 2004; Washburn et al., 2003; Washburn et al., 2001) and GPS benchmarks (Chen et al., 2004; Shen et al., 2001; Zhang et al., 2004). (c) Comparison of Altyn Tagh (after Liu, 1988) and San Andreas (after Dickinson, 1996) fault systems at same scale.

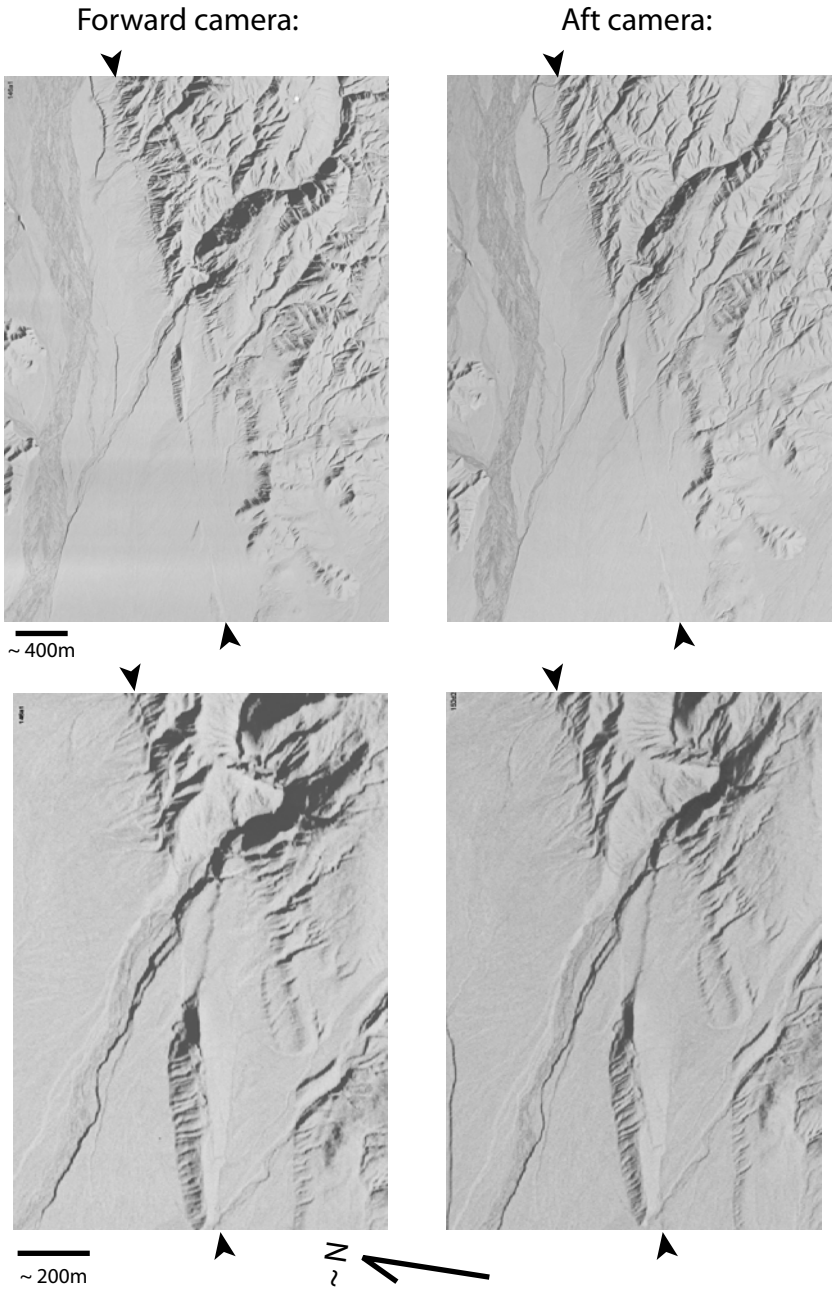

Figure DR2. Corona stereopairs showing the Yuemake site. Both overview (top) and detailed (bottom) views are shown. Arrowheads at top and bottom of each image point along the active trace of the ATF. Scenes are not georeferenced or rectified, thus scale bars and orientations are both approximate. Images were taken November 6, 1968 by the Corona program (http://www.nro.gov/corona/facts.html) and were obtained from the United States Geological Survey Earth Resources Observation and Science (EROS) Data Center (http://edc.usgs.gov/). Scene identification numbers are DS1105-1039F146 and DS1105-1039A152 for the forward and aft scenes, respectively.

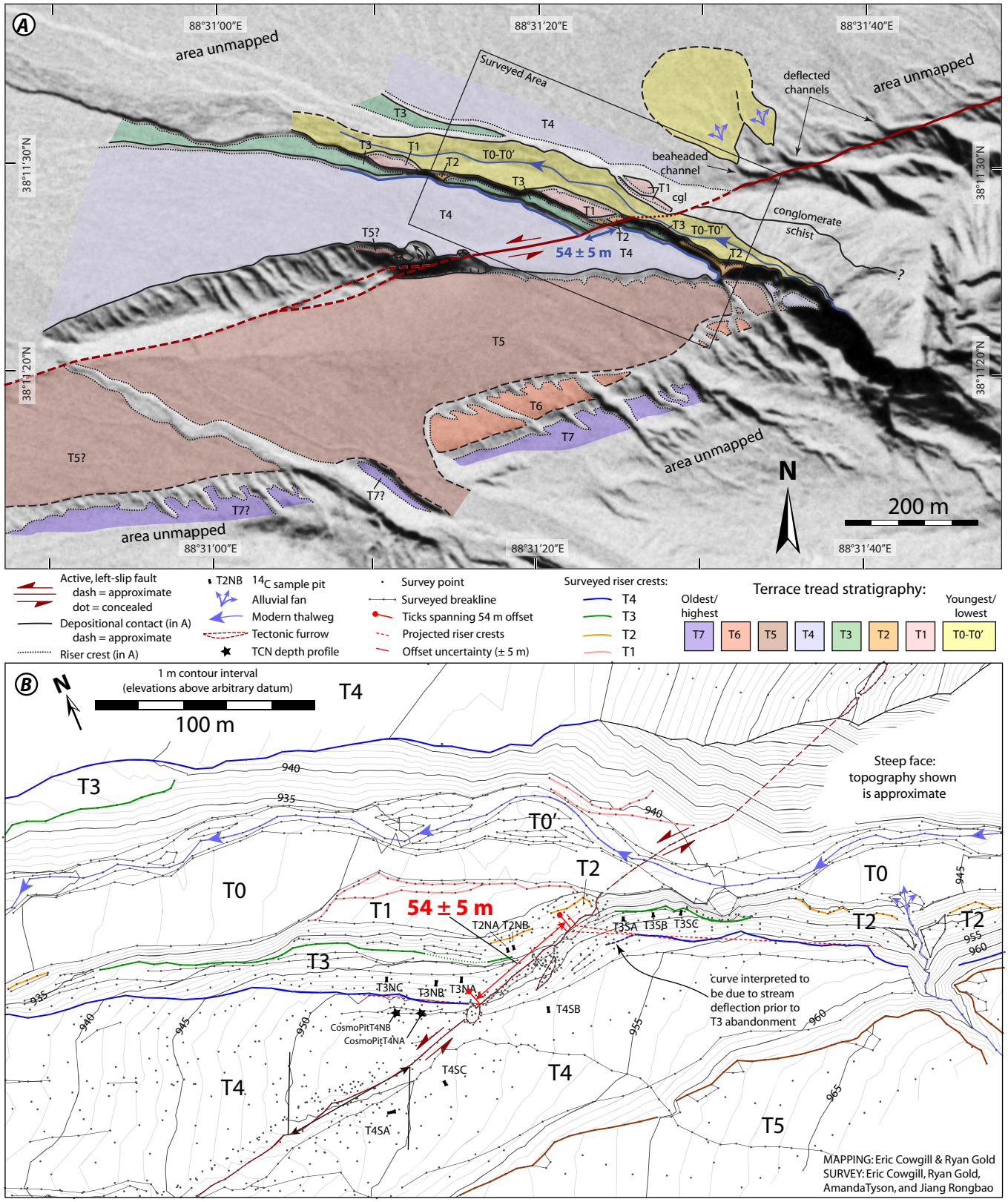
A
88°31′00″E
88°31′20″E
88°31′40″E
38°11′30″N
38°11′20″N
area unmapped
Surveyed Area
deflected channels
beaheaded channel
conglomerate
schist
cgl
T0-T0′
T1
T2
T3
T4
T5
T6
T7
T5?
T7?
54 ± 5 m
N
200 m
Active, left-slip fault
dash = approximate
dot = concealed
Depositional contact (in A)
dash = approximate
Riser crest (in A)
T2NB 14C sample pit
Alluvial fan
Modern thalweg
Tectonic furrow
TCN depth profile
Survey point
Surveyed breakline
Ticks spanning 54 m offset
Projected riser crests
Offset uncertainty (± 5 m)
Surveyed riser crests:
T4
T3
T2
T1
Terrace tread stratigraphy:
Oldest/ highest
Youngest/ lowest
T7
T6
T5
T4
T3
T2
T1
T0-T0′
B
N
1 m contour interval
(elevations above arbitrary datum)
100 m
Steep face:
topography shown
is approximate
T2NA T2NB
T3SA T3SB T3SC
T3NC T3NB T3NA
T4SB
T4SC
T4SA
CosmoPitT4NB
CosmoPitT4NA
curve interpreted to
be due to stream
deflection prior to
T3 abandonment
MAPPING: Eric Cowgill & Ryan Gold
SURVEY: Eric Cowgill, Ryan Gold,
AmandaTyson, and Jiang Rongbao

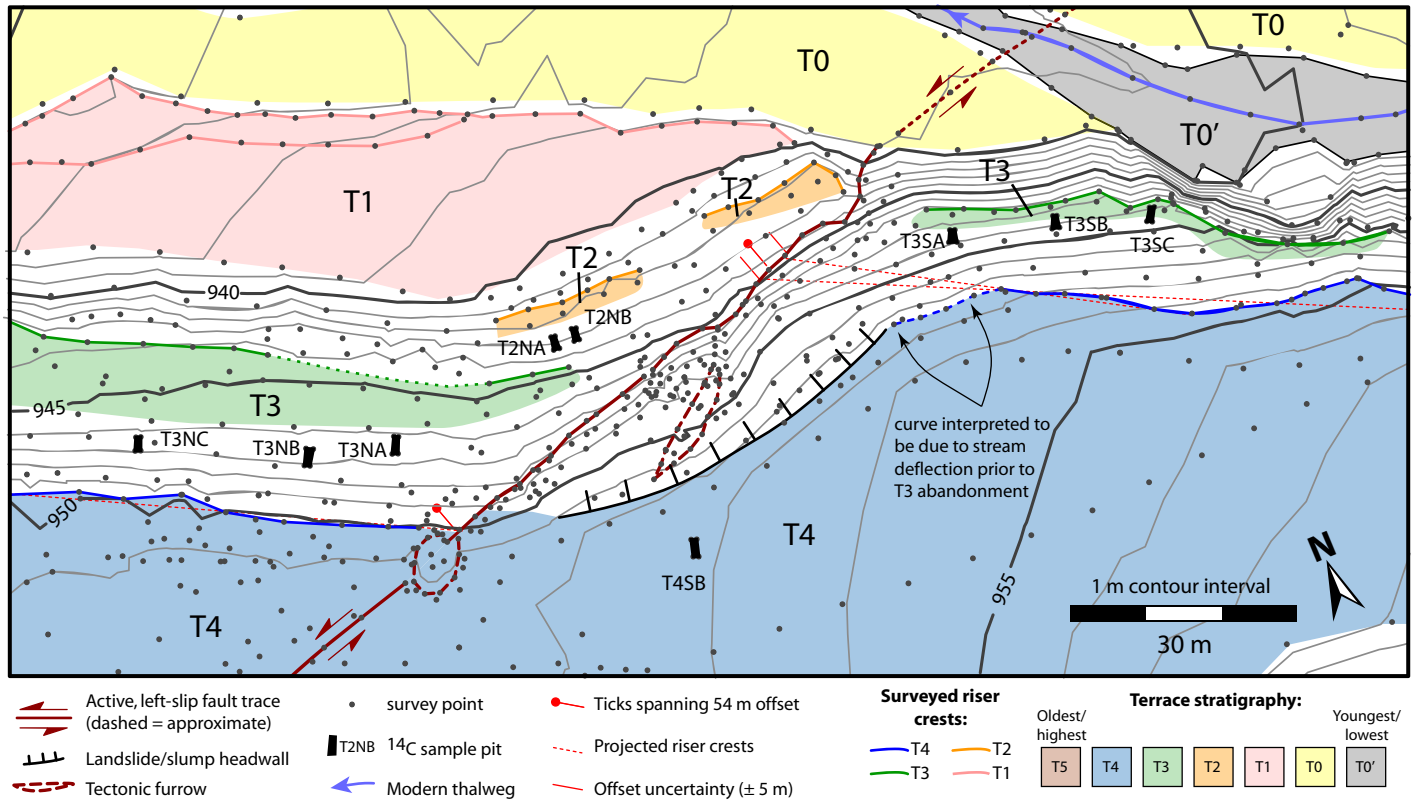

Figure DR3 (this page and previous). (a) Neotectonic map of Yuemake. Riser crests and bases are shown as dotted and dashed black lines, respectively, except for T4/T3 crest (solid blue line). Box outlines area of survey shown in part b and Fig. 2. (b) Survey data used to generate Fig. 2, including survey points (dots), breaklines (black and colored lines), and topographic contours. Riser crests are shown as solid, undecorated, colored lines. Thin red lines along crest of T4/T3 riser show range of possible projections into fault trace, with box indicating ±5 m uncertainty in displacement measurement. Stars labeled "CosmoPit" denote locations of depth profiles sampled, but not analyzed, for terrestrial cosmogenic nuclide (TCN) work. (c) Detailed view of survey data and site map showing fault trace, displaced riser crests and projections of the riser crests.

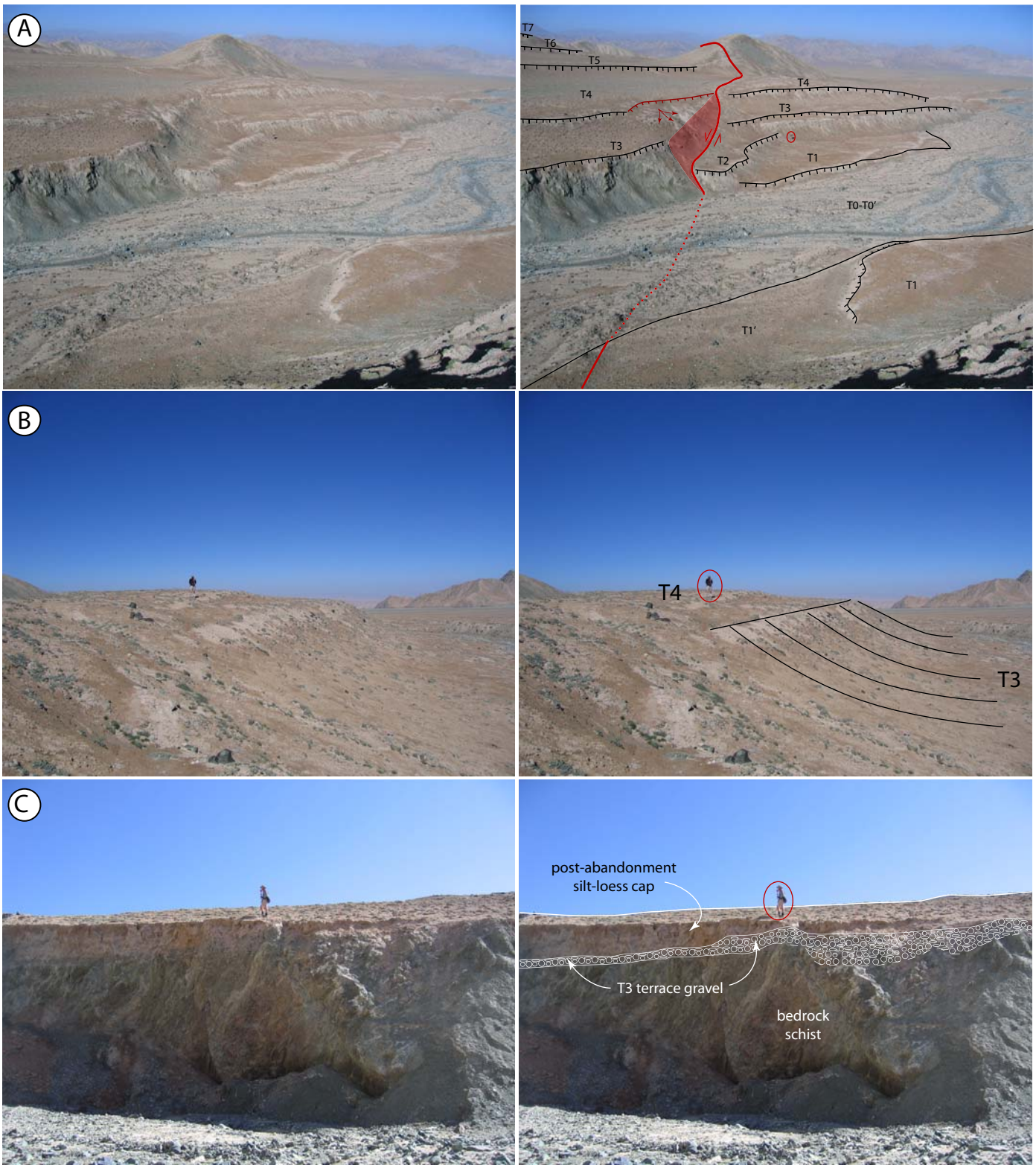

Figure DR4. Photos of key field relations; red circles indicate person for scale. (a) View to west-southwest of the ATF (red line) and displaced fluvial terraces along the west bank of the Yuemake channel. Red band indicates fault scarp. Black lines indicate crests of terrace risers with ticks on riser face. Ticked red line indicates approximate position of headwall of slump along ATF scarp. (b) View to north-northwest showing the profile of the T4/T3 fluvial riser north of the ATF. Riser face is asymmetric, with a steeper slope at the crest than the base. (c) View to west-southwest of the T3/T0 riser along the west bank of the Yuemake channel indicating that the T3 terrace is a strath cut into bedrock schist with ~1 m of fluvial conglomerate. The terrace is capped by ~1-2 m of loess deposited after tread abandonment.

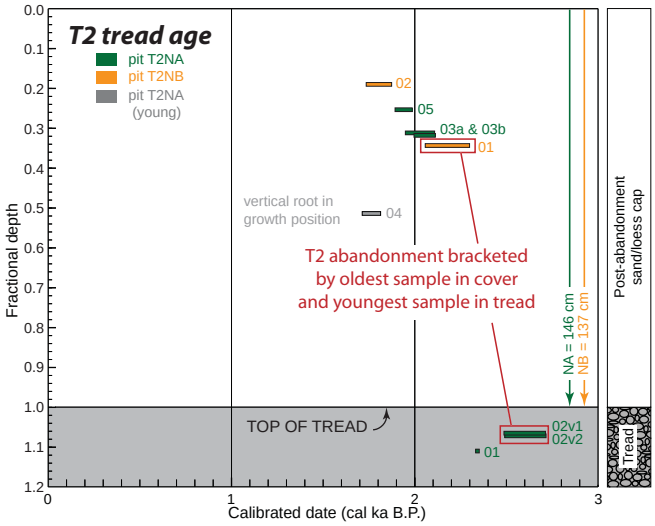

Figure DR5. Calibrated 14C dates (2σ) as a function of fractional depth into the terrace for T2. Fractional depth = 1 indicates the top of the abandoned terrace. Samples with fractional depth > 1.0 were collected from within the tread conglomerate and thus predate the time of tread abandonment. Samples with fractional depths < 1.0 were collected from within the post-abandonment capping loess deposit and thus postdate tread abandonment. These samples indicate that the T2 terrace was abandoned between 2354 and 2060 yr calBP. Note that not only are individual samples within stratigraphic order within the tread but that the sequence of T4, T3, and T2 abandonment ages is also in correct relative order.

References:

Bendick, R., Bilham, R., Freymueller, J., Larson, K., and Yin, G., 2000, Geodetic evidence for a low slip rate in the Altyn Tagh fault system: Nature, v. 404, p. 69-72.

Bronk Ramsey, C., 1995, Radiocarbon calibration and analysis of stratigraphy: The OxCal program: Radiocarbon, v. 37, p. 425-430.

—, 2001, Development of the radiocarbon calibration program OxCal: Radiocarbon, v. 43, p. 355-363.

Chen, Q., Freymueller, J., Wang, Q., Yang, Z., Xu, C., and Liu, J., 2004, A deforming block model for the present-day tectonics of Tibet: Journal of Geophysical Research, v. 109, p. doi:10.29/2002JB002151.

Cowgill, E., 2007, Impact of riser reconstructions on estimation of secular variation in rates of strike-slip faulting: revisiting the Cherchen River site along the Altyn Tagh Fault, NW China: Earth and Planetary Science Letters, v. 254, p. 239-255, doi:10.1016/j.epsl.2006.09.015.

Cowgill, E., Arrowsmith, J.R., Yin, A., Wang, X.-F., and Chen, Z., 2004a, The Akato Tagh bend along the Altyn Tagh fault, NW Tibet 2: Active deformation and the importance of transpression and strain hardening within the Altyn Tagh system: Geological Society of America Bulletin, v. 116, p. 1443-1464; doi: 10.1130/B25360.1.

Cowgill, E., Yin, A., Arrowsmith, J.R., Wang, X.-F., and Zhang, S., 2004b, The Akato Tagh bend along the Altyn Tagh fault, NW Tibet 1: Smoothing by vertical-axis rotation and the effect of topographic stresses on bend-flanking faults: Geological Society of America Bulletin, v. 116, p. 1423-1442; doi: 10.1130/B25359.1.

Dickinson, W.R., 1996, Kinematics of transrotational tectonism in the California Transverse Ranges and its contribution to cumulative slip along the San Andreas transform fault system, Geological Society of America Special Paper 305, p. 46 p.

England, P., and Molnar, P., 2005, Late Quaternary to decadal velocity fields in Asia: Journal of Geophysical Research, v. 110, p. doi:10.1029/2004JB003541.

Ge, S., Shen, G., Wei, R., Ding, G., and Wang, Y., 1992, Active Altun fault zone monograph (in Chinese with English abstract): Beijing, P.R. China, State Seismological Bureau of China, 319 p.

Gold, R.D., Cowgill, E., Arrowsmith, J.R., Gosse, J., Chen, X., and Wang, X.-F., in press, Riser diachroneity, lateral erosion, and uncertainty in rates of strike-slip faulting: A case study from Tuzidun along the Altyn Tagh Fault, NW China: Journal of Geophysical Research, p. doi:10.1029/2008JB005913.

Harkins, N., and Kirby, E., 2008, Fluvial terrace riser degradation and determination of slip rates on strike-slip faults: An example from the Kunlun fault, China: Geophysical Research Letters, v. 35, p. doi:10.1029/2007GL033073.

Lacassin, R., Valli, F., Arnaud, N., Leloup, P.H., Paquette, J.L., Li, H., Tapponnier, P., Chevalier, M.-L., Guillot, S., Maheo, G., and Xu, Z., 2004, Large-scale geometry, offset and kinematic evolution of the Karakorum fault, Tibet: Earth and Planetary Science Letters, v. 219, p. 255-269.

Liu, Z.Q., 1988, Geologic Map of the Qinghai-Xizang Plateau and its Neighboring Regions (in Chinese): Beijing, Chengdu Institute of Geology and Mineral Resources, Academica Sinica Geology Publisher.

Mériaux, A.-S., Ryerson, F.J., Tapponnier, P., Van der Woerd, J., Finkel, R.C., Xu, X., Xu, Z., and Caffee, M.W., 2004, Rapid slip along the central Altyn Tagh Fault:

morphochronologic evidence from Cherchen He and Sulamu Tagh: Journal of Geophysical Research, v. 109, p. DOI:10/1029/2003jb002558.
Mériaux, A.-S., Tapponnier, P., Ryerson, F.J., Xu, X., King, G., Van der Woerd, J., Finkel, R.C., Li, H., Caffee, M.W., Xu, Z., and Chen, W., 2005, The Aksay segment of the northern Altyn Tagh fault: tectonic geomorphology, landscape evolution, and Holocene slip rate: Journal of Geophysical Research, v. 110, p. doi: 10.1029/2004JB003210.
Muretta, M., Arrowsmith, J.R., Gold, R.D., Cowgill, E., Chen, X., and Wang, X.F., 2007, Paleoearthquake history of the Cherchen He reach of the central Altyn Tagh Fault, Xinjiang China: Eos Transactions, American Geophysical Union, v. 88, p. Abstract G21C-0669.
Murphy, M.A., and Burgess, W.P., 2006, Geometry, kinematics, and landscape characteristics of an active transtension zone, Karakoram fault system, Southwest Tibet: Journal of Structural Geology, v. 28, p. 268-283.
Olsson, I.U., 1986, Radiometric Methods, *in* Berglund, B.E., ed., Handbook of Holocene palaeoecolgy and palaeohydrology, John Wiley & Sons, Chichester, p. 273-312.
Peltzer, G., Tapponnier, P., and Armijo, R., 1989, Magnitude of late Quaternary left-lateral movement along the north edge of Tibet: Science, v. 246, p. 1285-1289.
Reimer, P., Baillie, M., Bard, E., Bayliss, A., Beck, J., Bertrand, J., Blackwell, P., Buck, C., Burr, G., Cutler, K., Damon, P., Edwards, R., Fairbanks, R., Friedrich, M., Guilderson, T., Hogg, A., Hughen, K., Kromer, B., McCormac, G., Manning, S., Ramsey, C.B., Reimer, R., Remmele, S., Southon, J., Stuiver, M., Talamo, S., Taylor, F., Plicht, J.v.d., and Weyhenmeyer, C., 2004, IntCal04 terrestrial radiocarbon age calibration, 0-26 cal kyr BP: Radiocarbon, v. 46, p. 1029-1058.
Shen, F., Royden, L.H., and Burchfiel, B.C., 2001, Large-scale crustal deformation of the Tibetan Plateau: Journal of Geophysical Research, v. 106, p. 6793-6816.
Stuiver, M., and Polach, H.A., 1977, Reporting of 14C data: Radiocarbon, v. 19, p. 355-363.
Tapponnier, P., Xu, Z., Roger, F., Meyer, B., Arnaud, N., Wittlinger, G., and Yang, J., 2001, Oblique stepwise rise and growth of the Tibet Plateau: Science, v. 294, p. 1671-1677.
Taylor, M., Yin, A., Ryerson, F.J., Kapp, P., and Ding, L., 2003, Conjugate strike-slip faulting along the Bangong-Nujiang suture zone accommodates coeval east-west extension and north-south shortening in the interior of the Tibetan Plateau: Tectonics, v. 22, p. doi:10.1029/2002TC001361.
Thatcher, W., 2007, Microplate model for the present-day deformation of Tibet: Journal of Geophysical Research, v. 112, p. doi:10.1029/2005jb004244.
Van der Woerd, J., Ryerson, F.J., Tapponnier, P., Gaudemer, Y., Finkel, R., Meriaux, A.S., Caffee, M., Zhao, G., and He, Q., 1998, Holocene left-slip rate determined by cosmogenic surface dating on the Xidatan segment of the Kunlun fault (Qinghai, China): Geology, v. 26, p. 695-698.
Van der Woerd, J., Tapponnier, P., Ryerson, F.J., Meriaux, A.-S., Meyer, B., Gaudemer, Y., Finkel, R.C., Caffee, M.W., Zhao, G., and Xu, Z., 2002, Uniform postglacial slip-rate along the central 600 km of the Kunlun fault (Tibet), from 26Al, 10Be and 14C dating of riser offsets, and climatic origin of the regional morphology: Geophysical Journal International, v. 148, p. 356-388.
Wallace, K., Yin, G., and Bilham, R., 2004, Inescapable slow slip on the Altyn Tagh fault: Geophysical Research Letters, v. 31, p. doi:10.1029/2004GL019724.

Washburn, Z., Arrowsmith, J.R., Dupont-Nivet, G., Wang, X.-F., Zhang, Y.-Q., and Chen, Z., 2003, Paleoseismology of the Xorxol segment of the Central Altyn Tagh Fault, Xinjiang, China: Annals of Geophysics, v. 5, p. 1015-1034.

Washburn, Z., Arrowsmith, J.R., Forman, S.L., Cowgill, E., Wang, X., Zhang, Y., and Chen, Z., 2001, Late Holocene earthquake history of the central Altyn Tagh Fault, China: Geology, v. 29, p. 1051-1054.

Yin, A., McRivette, M.W., Burgess, W.P., and Chen, X., 2007, Cenozoic tectonic evolution of Qaidam basin and its surrounding regions (Part 2): Wedge tectonics in southern Qaidam basin and the Eastern Kunlun Range, *in* Sears, J.W., Harms, T.A., and Evenchick, C.A., eds., Whence the Mountains? Inquiries into the evolution of orogenic systems: A volume in honor of Raymond A. Price: Boulder, CO, Geological Society of America Special Paper 433, p. 369–390, doi: 10.1130/2007.2433(18).

Zhang, P.-Z., Molnar, P., and Xu, X., 2007, Late Quaternary and present-day rates of slip along the Altyn Tagh Fault, northern margin of the Tibetan Plateau: Tectonics, v. 26, p. TC5010, doi:10.1029/2006TC002014.

Zhang, P.-Z., Shen, Z., Wang, M., Gan, W., Bürgmann, R., Molnar, P., Wang, Q., Niu, Z., Sun, J., Wu, J., Sun, H., and You, X., 2004, Continuous deformation of the Tibetan Plateau from global positioning system data: Geology, v. 32, p. 809-812; doi:10.1130/G20554.1.